JACS
JOURNAL OF THE AMERICAN CHEMICAL SOCIETY
pubs.acs.org/JACS
Article

General Route to Colloidally Stable, Low-Dispersity Manganese-Based Ternary Spinel Oxide Nanocrystals

Jonathan L. Rowell, Yafu Jia, Zixiao Shi, Andrés Molina Villarino, Minsoo Kang, Dasol Yoon, Kevin Zhijian Jiang, Héctor D. Abruña, David A. Muller, and Richard D. Robinson*

Cite This: J. Am. Chem. Soc. 2023, 145, 17406−17419

Read Online

ACCESS | Metrics & More | Article Recommendations | Supporting Information

ABSTRACT: While certain ternary spinel oxides have been well-explored with colloidal nanochemistry, notably the ferrite spinel family, ternary manganese (Mn)-based spinel oxides have not been tamed. A key composition is cobalt (Co)-Mn oxide (CMO) spinel, $Co_xMn_{3-x}O_4$, that, despite exemplary performance in multiple electrochemical applications, has few reports in the colloidal literature. Of these reports, most show aggregated and polydisperse products. Here, we describe a synthetic method for small, colloidally stable CMO spinel nanocrystals with tunable composition and low dispersity. By reacting 2+ metal-acetylacetonate ($M(acac)_2$) precursors in an amine solvent under an oxidizing environment, we developed a pathway that avoids the highly reducing conditions of typical colloidal synthesis reactions; these reducing conditions typically push the system toward a monoxide impurity phase. Through surface chemistry studies, we identify organic byproducts and their formation mechanism, enabling us to engineer the surface and obtain colloidally stable nanocrystals with low organic loading. We report a CMO/carbon composite with low organic contents that performs the oxygen reduction reaction (ORR) with a half-wave potential ($E_{1/2}$) of 0.87 V vs RHE in 1.0 M potassium hydroxide at 1600 rpm, rivaling previous reports for the highest activity of this material in ORR electrocatalysis. We extend the general applicability of this procedure to other Mn-based spinel nanocrystals such as Zn-Mn-O, Fe-Mn-O, Ni-Mn-O, and Cu-Mn-O. Finally, we show the scalability of this method by producing inorganic nanocrystals at the gram scale.

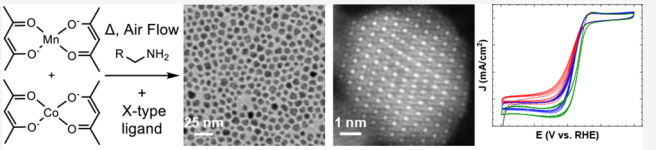

- No aggregates
- Small (<10 nm)
- Low dispersity (<20 %)
- Colloidally stable
- Gram-scale synthesis
- Composition control
- General to Mn-spinels
- High ORR activity

INTRODUCTION

The synthesis of ternary spinel oxide nanocrystals is increasingly being pursued due to the diverse applications of these materials.[1−3] Manganese (Mn) ternary spinels have been targeted for a variety of energy applications such as supercapacitors,[4−9] lithium-ion batteries,[10−14] and as electrocatalysts for the oxygen reduction reaction (ORR)[15−27] and the oxygen evolution reaction (OER).[19−21,27−29] Cobalt-manganese (Co-Mn) spinel oxides, in particular, have demonstrated outstanding performance as supercapacitors and electrocatalysts.[6,8,15−18,25,27,29,30] The normal spinel structure is AB_2O_4, where A is a 2+ cation with tetrahedral coordination and B is a 3+ cation with octahedral coordination; in inverse spinels, the 2+ cation occupies an octahedral site and half of the 3+ cations occupy the tetrahedral site; and in complex spinels, a mixture of normal and inverse spinel structures exists.[1] Previous work on Co-Mn spinels suggests that it is a complex spinel structure.[7] The performance of Co-Mn spinel nanomaterials used in energy applications is highly dependent on the intrinsic physical properties of the material, such as the electronic conductivity and the binding of reaction intermediates to the nanocrystal surface.[16,24,27,31,32] The physical properties of nanomaterials, in turn, are strongly dependent on particle size and morphology due to the influence of properties such as quantum confinement, surface and/or lattice strain,[33−36] or the geometric increase in the surface area-to-volume ratio at small sizes.[37,38] Thus, the ideal testbed to study these materials and their applications is in the form of low-dispersity nanocrystals with a controllable size. Control of composition, size, and low dispersity is critical for generating accurate correlations between physical properties and application performance and for enabling tunable properties for the desired application.

To the best of our knowledge, the current research of ternary Mn spinels, however, has been unable to develop synthetic methods to produce small, colloidally stable, low-dispersity nanocrystals. Of particular interest is the CMO family of spinels, known for their superior electrocatalytic and supercapacitor performance.[6,8,15−18,25,27,29,30] Previous work

Received: May 31, 2023
Published: August 1, 2023

https://doi.org/10.1021/jacs.3c05706
J. Am. Chem. Soc. 2023, 145, 17406−17419

using hydrothermal/solvothermal,[16−18] solid-state,[26,27,29] co-precipitation,[20,30,39] or solvent-assisted[24,25,31] methods to generate CMO spinels has resulted in large,[16,17,19,20,27,31] aggregated[21,25,26,28,39] nanocrystals with poor size control. Additionally, methods like solvothermal and hydrothermal reactions make optimization and scaling more difficult because of the need for a pressurized vessel, which leads to the inability to take reaction aliquots, thus restricting the determination of the onset of Ostwald ripening.[16−18]

The colloidal heat-up synthesis technique offers the ability to produce small, monodisperse nanocrystals *via* a highly scalable procedure.[40,41] In addition, the amphiphilic ligands—with polar head groups and long alkyl chains—used in colloidal syntheses separate the particles and prevent uncontrolled growth and aggregation.[41] One factor that may be precluding the development of methods for colloidal CMO spinel nanocrystals is the fact that the typical environments of oxide nanocrystal syntheses are reducing in nature. Such reactions are generally run at high temperature, in an inert atmosphere, and in reducing solvents like amines or alcohols.[42−44] Spinels fill their octahedral and tetrahedral sites with a mix of higher and lower oxidation state cations (i.e., 2+ and 3+).[1] It is likely that this reducing environment prevents the range of higher oxidation state cations, leading to the preferential formation of the rock-salt phase over the spinel phase. Of the ternary spinels, colloidal synthesis of ferrite spinels[2,23,42,43,45−48] has been the most successful, likely because of the thermodynamic preference of the Fe cation for the 3+ state due to the lower formal potential of its Fe 2+/3+ redox couple (0.77 V vs NHE) compared to other spinel transition metal cations such as Mn and Co (1.50 and 1.92 V vs NHE, respectively).[49] This lower reduction potential for the Fe 2+/3+ couple is likely why Fe cations are not reduced in the presence of amine[42,44] and alcohol ligands[42,43,50,51] at the high temperatures typical of colloidal syntheses. Of the few colloidal Co-Mn spinel nanocrystal syntheses reported in the literature,[6,9,21,28,52] all contain aggregates to some degree, none have demonstrated compositional control, and many are difficult to reproduce[52] (likely due to the impurity of the amine ligand used in synthesis, as we address later; *vide infra*). Finally, procedures using oleylamine (OLAM) as a ligand tend to produce high-molecular-weight organic byproducts which increase electrochemical impedance and negatively alter surface chemistry.[52−54]

In this work, we present the synthesis of small (<10 nm), low-dispersity (<20%), colloidally stable CMO spinel nanocrystals with compositional control of 0−60% cobalt. The synthesis uses low-cost precursors, is performed at moderate temperatures (<230 °C), and is a one-step ("heat-up" synthesis) procedure. We find that the key component to forming the spinel phase is to react metal-acetylacetonate precursors in an oxidizing environment of dry air—to aid the cation oxidation that is necessary to form the spinel phase—with an amine ligand as the solvent. Through surface chemistry studies, we identify issues with previous methods that result in poor passivation and particle aggregation[21,28] and lead to high-molecular-weight byproducts that impede electrocatalytic activity. We overcome these challenges to enable colloidally stable nanocrystals, with high electrocatalytic performance. Since the synthesis is a simple heat-up method, it is highly scalable, and we are able to achieve gram-scale syntheses. Finally, we empirically show that this method is generally applicable to other Mn-based spinels and other amine ligands.

The general synthetic strategy (Scheme 1) involves the thermal decomposition of an equimolar ratio of $Co(acac)_2$ and

Scheme 1. General Synthetic Route to CMO Spinel Nanocrystals

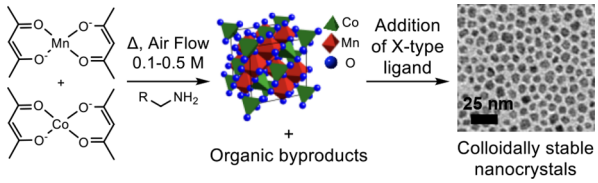

$Mn(acac)_2$ complexes in a medium of alkylamines under an air atmosphere. The essential path to forming the spinel phase is oxidation of the 2+ precursors, with molecular oxygen acting as the terminal oxidant. We believe that the amine, along with operating as a nucleophile that induces the decomposition of the metal-acac precursor,[44] acts as a redox mediator in the reaction that enables the aerobic oxidation of the 2+ cations. Despite obtaining the desired product of spinel oxide nanocrystals, the oxidation of ligands leads to the generation of various organic byproducts. Moreover, the decomposition of the ligands exhausts the initial L-type amine ligand, resulting in under-passivated colloids that lack stability and tend to aggregate after multiple washes needed to eliminate higher molecular weight byproducts. Through the addition of an X-type ligand, the nanocrystals become colloidally stable, even after the multiple washes. Through the use of relatively short alkyl chain ligands (octylamine), the overall organic loading is lowered—due to decreased hydrophobicity related to the shorter aliphatic chain length—in both the resultant nanocrystals and in the nanocrystal-carbon composites employed in electrochemical applications, thus leading to both higher performance and stability for ORR catalysis.

EXPERIMENTAL SECTION

Materials. For nanocrystal synthesis and post-treatment, cobalt(II) acetylacetonate ($Co(acac)_2$,≥99.0%), manganese(II) acetylacetonate ($Mn(acac)_2$), OLAM (≥98% primary amine), and octylamine (99%) were purchased from Sigma-Aldrich. OLAM was vacuum distilled over calcium hydride (purchased from Sigma Aldrich) prior to use to remove possible impurities and water. Hexane (≥98.5%) was purchased from VWR Chemicals, and acetone (ACS grade, ≥95%) was purchased from Macron Fine Chemicals. Chloroform (ACS grade) was purchased from Fisher Scientific. Lauric acid ($CH_3(CH_2)_{10}COOH$, lab grade) was purchased from Ward's Science. Nitric acid (70%, redistilled, ≥99.999%) was purchased from Sigma Aldrich. DI H_2O was obtained from a 7148 Thermo Scientific Barnstead Nanopure purification system (18.2 MΩ cm). High surface area carbon black (KETJENBLACK EC-300J) was purchased from Akzo Nobel Functional Chemicals LLC.

For electrochemical testing, diamond paste (diamond polishing compound; 1 μm), MetaDi Fluid (extender for diamond abrasives), and polishing cloth (Microcloth) were purchased from BUEHLER. Ar (100%; UHP300) and O_2 (100%; UHP300) were purchased from Airgas. Nafion solution (DUPONT D2021 Nafion Solution) was purchased from Ion Power.

Synthesis of $Co_xMn_{3-x}O_4$ Nanocrystals in OLAM. To synthesize CMO nanocrystals, 3 mmol $Co(acac)_2$ (771 mg), 3 mmol $Mn(acac)_2$ (759 mg), and 12 mL of OLAM were mixed in a 50 mL three-neck flask with magnetic stirring. The reaction mixture was heated to 70 °C and subjected to vacuum for 1 h to remove possible water and impurities. After degassing, a blunt-end needle was inserted to the flask to purge air through the reaction with a flow rate of 10−20 cc/min. The air flow was passed through Drierite to ensure the

https://doi.org/10.1021/jacs.3c05706
J. Am. Chem. Soc. 2023, 145, 17406−17419

removal of moisture. The solution was then heated to 130 °C at a ramp rate of 4 °C/min over 15 min and kept at 130 °C for 40 to 120 min. The reaction was terminated by quenching in a water bath. The purification of the nanoparticle surface is described in the following section. The experimental conditions (solvent/ligand, precursor purification, final temperature, soak time, air flow rate) were modified based on different synthetic goals, and the details of control parameters can be found in Table S1 in the Supporting Information. Note: the TEM image was taken after full purification of the nanocrystals to a dry powder (except for the fully Mn spinel, taken from an aliquot at the end of the reaction), followed by re-dispersion of the powder in hexanes and drop-casting on the TEM grid.

Synthesis of CMO Nanocrystals in Octylamine. The synthesis method that uses octylamine as the surfactant is similar to the method described above. However, the degassing strategy was different from the last section due to the lower boiling point of octylamine, and the method is described below.

To synthesize CMO nanocrystals in octylamine, 1.5 mmol $Co(acac)_2$ (386 mg) and 1.5 mmol $Mn(acac)_2$ (380 mg) were placed in a 50 mL round-bottom flask, and vacuum was pulled to approximately 10 mTorr. The flask was refilled with nitrogen, 20 mL of octylamine (98% purity or higher) was added, and the flask contents were mixed in a 50 mL three-neck flask with magnetic stirring. The flask was then put back under vacuum for 15 min at room temperature (RT) or purged with nitrogen at 70 °C. After degassing, a 16-gauge 15 cm needle was inserted to purge air through the reaction with a flow rate of 10−20 cc/min. The air-line was passed through Drierite to ensure the removal of moisture. The solution was then immediately heated to 160 °C at a ramp rate of 4 °C/min over 32.5 min and kept at 160 °C for 20 to 30 min. During the heat-up, the needle for the air-flow was placed to bubble through the solution once all precursors dissolved. The reaction is terminated by quenching the flask in a water bath.

Purification of CMO Nanocrystals. To re-passivate the surface, 1 g of lauric acid was dissolved in 2 mL of hexanes at moderate temperature and introduced to the reaction solution after cooling down the reaction (similar procedure when particles are re-passivated with amines). The mixture was sonicated for 5 min and then centrifuged at 6000 rpm for 10 min. After centrifugation, only the supernatant was taken out and used for further washes. We believe that the precipitates consisted of high-molecular-weight organic byproducts which negatively influence the nanoparticle performance for further applications along with a small amount of nanocrystal product. Antisolvent (acetone) was added to the supernatant until flocculation was observed. The supernatant was then centrifuged at 8500 rpm for 10−15 min. In the next wash, the nanocrystals were dispersed in hexane and then precipitated with acetone. The mixture was centrifuged again at 8500 rpm for 15 min. This step was repeated once or twice to obtain nanocrystals with low organic loading.

Processing of Catalyst Composites. 35 mg of Ketjenblack (KB) was added into 10 mL of chloroform, and the solution was sonicated for 1 h. CMO nanocrystals (65 mg) were dispersed in 10 mL of chloroform. The dispersed nanoparticle was slowly injected into the carbon black solution at a rate of 1 mL/min under a nitrogen atmosphere while magnetically stirring. The combined solution was then sonicated for another 1 h. The chloroform was subsequently removed by heating (plate) at around 40 °C while purging nitrogen through the vessel. The dried product was ground to form a homogeneous powder. Lastly, the powder was heat-treated in a furnace at 175 °C for 17 h in air to remove the surface-capping agent.

Characterization. *Powder X-ray Diffraction (PXRD).* The diffraction patterns of synthesized nanocrystals were obtained on a Bruker D8 Advance ECO powder diffractometer with a Cu K_α (1.5406 Å) X-ray source. The nanocrystals were ground into a fine powder before the measurement to exclude any preference on crystal orientation. The 2-θ value ranged from 25 to 75°, where the most intense peaks are found. The step size of each measurement is 0.05°, and each step is measured for 1.5 s.

Low-Magnification Transmission Electron Microscopy (TEM). The nanocrystals were dispersed in hexane and drop-cast onto a carbon-coated copper TEM grid. The grid was covered by a petri dish during the evaporation of hexane to avoid coffee ring effects. TEM images were obtained at room temperature using a Tecnai 12 BioTwin transmission electron microscope (Fei Company; Hillsboro, OR), with a LaB_6 electron source operated at 120 kV, and a Gatan Orius S1000 CCD camera. Particle distributions were measured from these images using ImageJ (https://imagej.nih.gov/ij/download.html).

Annular Bright-Field Scanning Transmission Electron Microscopy (ABF-STEM), High-Angle Annular Dark-Field (HAADF) STEM, and Elemental Mapping. STEM images and electron energy loss spectroscopy (EELS) data were collected on a FEI Titan Themis (S)TEM operating at 120 kV with a Gatan GIF Quantum 965 spectrometer and on a Thermo Fisher Scientific Spectra 300 X-CFEG operating at 200 kV. The chemical composition maps were obtained by integrating the signal from the Co and Mn $L_{2,3}$ edges after background subtraction using a power law background fit.

Nuclear Magnetic Resonance (NMR). ^{1}H NMR spectra were collected using a 500 MHz Bruker AVIII with BBO Prodigy cryoprobe at the Cornell NMR and Chemistry Mass Spectrometry Facilities. NMR samples were prepared in chloroform-d. Quantitative ^{1}H spectra were collected over 4 scans with a 30 s relaxation delay and a 90° excitation pulse at room temperature, and ^{13}C spectra were collected with ^{1}H decoupling and 128 scans over 10 min.

Fourier Transform Infrared Spectroscopy (FTIR). Bonding conditions of reaction side products and surface ligands were studied using a Bruker Vertex V80V vacuum FTIR system in attenuated total reflectance (ATR) mode. The spectrum was measured from 700 to 4000 cm^{-1} with 256 scans in each measurement. Side products were purified by vacuum distillation and then drop-cast onto the ATR ruby crystal in air. The measured spectra were corrected by the background air spectrum to exclude the noise signal from ambient water and carbon dioxide.

Differential/Thermogravimetric Analysis (D/TGA). D/TGA measurements were performed using a TA5500 TGA (TA Instruments; New Castle, DE) at the Cornell Center for Materials Research (CCMR), with high-temperature Pt pans (100 μL). Measurements consisted of a linear temperature ramp (10 °C/min) from room temperature to 800 °C in an air atmosphere, with a gas flow rate of 15 mL/min. No weight stabilization induction time was employed to observe potential water desorption from hygroscopic surfaces.

X-ray Photoelectron Spectroscopy (XPS). XPS measurements were carried out using an Omicron ESCA 2SR instrument with a monochromatized Al K_α excitation source. XPS spectra were analyzed using the CasaXPS software. All binding energies (BEs) were calibrated using the C 1s peak. Shirley backgrounds were used to remove the background for the Co 2p and Mn 2p peaks. The extracted spectra were fitted with a 70% Gaussian/30% Lorentzian (GL(30)) line shape. The cobalt and manganese oxidation states were probed using XPS. The Mn 2p spectra were deconvolved into Mn^{2+} and Mn^{3+} signals. The peaks at 640.60 and 651.6 with a 11.05 eV separation[55] and a full width at half-maximum (FWHM) of 3.17 were assigned to Mn $2p_{3/2}$ and Mn $2p_{1/2}$ of Mn^{2+}, respectively. The peaks at 642.36 and 653.41 eV with an 11.05 eV separation and a FWHM of 3.70 eV were assigned to Mn $2p_{3/2}$ and Mn $2p_{1/2}$ of Mn^{3+}, respectively.[56−58] The Co 2p spectra were deconvolved into Co^{2+} and Co^{3+} signals with an additional satellite peak. The peaks at 781.01 and 795.98 eV with a 14.97 eV separation[55] and a FWHM of 2.63 were assigned to Co $2p_{3/2}$ and Co $2p_{1/2}$ of Co^{2+}, respectively. The peaks at 779.42 and 794.39 eV with a 14.97 eV separation[55] and a FWHM of 2.88 eV were assigned to Co $2p_{3/2}$ and Co $2p_{1/2}$ of Co^{3+}, respectively.[59−61]

Inductively Coupled Plasma-Atomic Emission Spectroscopy (ICP-AES). ICP-AES studies were performed by the Cornell Nutrient Analysis Laboratory (CNAL). For a typical powder sample, 2−5 mg of nanoparticles was placed in a clean 40 mL vial or a 50 mL centrifuge tube. ~1.5 mL of concentrated nitric acid was added to the vial, which was subsequently sonicated until no solids were seen in solution (~1−2 h). A portion of the solution was diluted 60−100× in DI water for analysis.

https://doi.org/10.1021/jacs.3c05706
J. Am. Chem. Soc. 2023, 145, 17406−17419

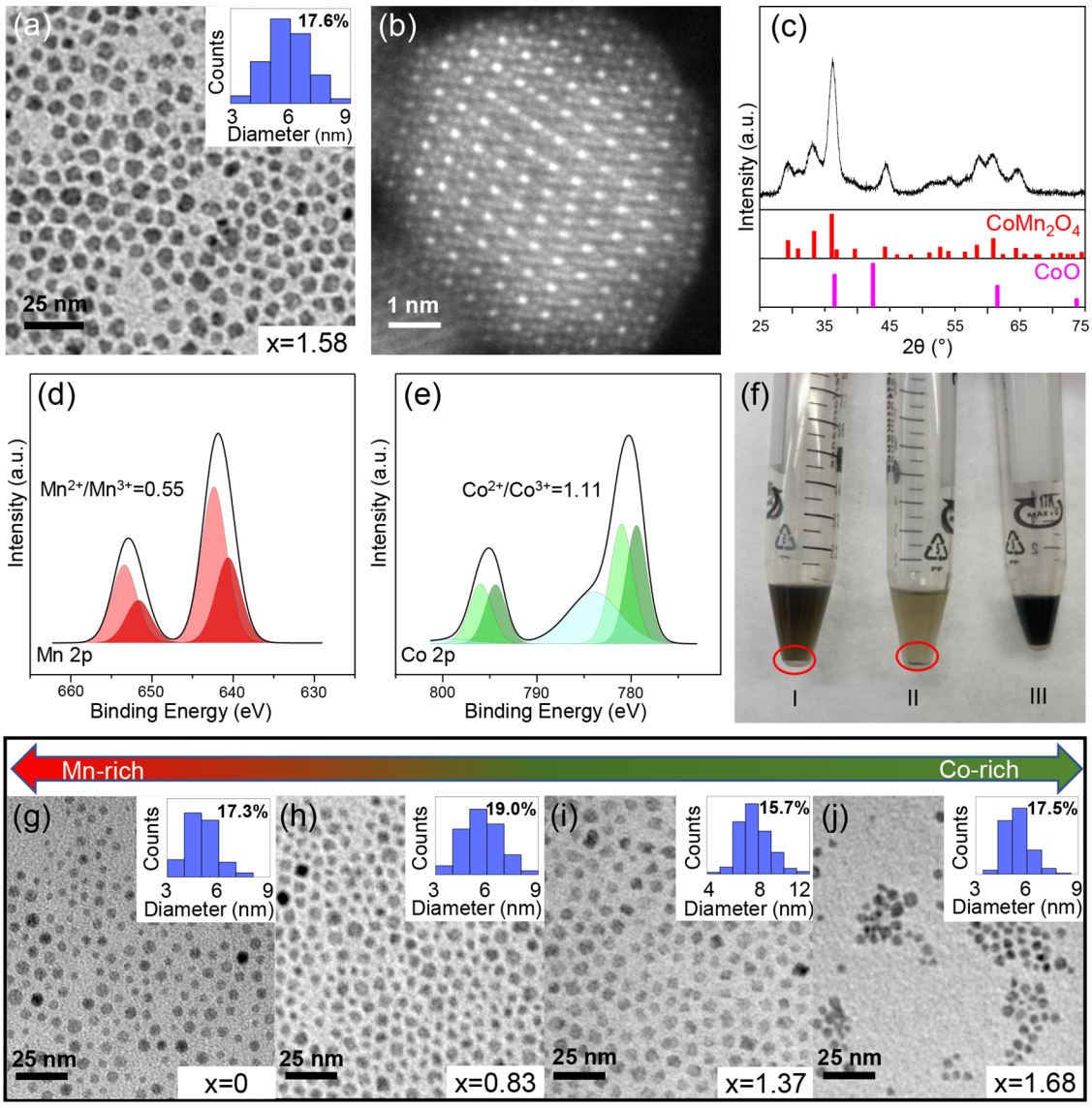

Figure 1. Characterization of $Co_xMn_{3-x}O_4$ (CMO) nanocrystals. (a) Low-magnification TEM image of typical nanocrystal synthesis in octylamine (reaction CMO-01). Inset shows particle size distribution, showing low-dispersity particles (17.6%). (b) HAADF-STEM of CMO nanocrystals, indicating that the particles are single crystalline with a spinel atomic structure. (c) PXRD patterns of CMO-02 peaks match those of spinel $CoMn_2O_4$ (red bars, JCPDS card file # 01-077-0471) and show no rock-salt oxide CoO (purple bars, JCPDS card file #00-009-0402). (d, e) Fitted XPS data from nanocrystals for the Mn 2p peak (d) and the Co 2p peak (e). The higher average oxidation state of the Mn cations suggests that they preferentially undergo the oxidative decomposition mechanism that enables the formation of the spinel phase. (f) Photograph of tubes of final nanocrystal products of reaction in octylamine solvent (CMO-04) with the following: (I) no ligand added at the end of the reaction, (II) octylamine added at the end of the reaction, and (III) lauric acid added at the end of the reaction. Only X-type lauric acid completely resolubilizes the nanocrystals. Precipitates are circled in red. (g–j) TEM images of compositional series of $Co_xMn_{3-x}O_4$ spinel nanocrystals for $x = 0$ (reaction MO-01) (g), $x = 0.83$ (reaction CMO-06) (h), $x = 1.37$ (reaction CMO-07) (i), and $x = 1.68$ (reaction CMO-08) (j). Inset shows statistical size distribution, showing uniform particle sets.

Inductively Coupled Plasma–Mass Spectrometry (ICP-MS). ICP-MS was conducted only for samples CMO-10, CMO-11, and CMO-14. All other compositions were derived from ICP-AES analysis. ICP-MS analysis was conducted independently by the Cornell Mass spectrometry (CMaS) Facility. 50–100 mg of dry nanocrystal powder was annealed for 24 h at 300 °C and then pressed into a pellet for analysis.

Electrochemical Setup and Voltammetry. Electrochemical tests were performed in a custom-made three-compartment glass RDE cell with a splashguard using a WaveDriver 20 bipotentiostat (Pine Research Instrumentation; Durham, NC) and an AFMSRCE electrode rotator (Pine Research Instrumentation; Durham, NC). No iR-drop corrections were performed during data acquisition nor processing. An AFE3T050GC glassy carbon RDE (Pine Research Instrumentation; Durham, NC), a carbon rod (GAMRY Instruments; Warminster, PA), and a KCl-saturated CHI111 Ag/AgCl electrode (CHI Instruments, Inc.; Austin, TX) served as the working, counter, and reference electrodes, respectively. The working electrode was manually polished to a mirror finish using diamond paste and MetaDi fluid on a polishing cloth. Reference potentials were converted to the RHE scale using the Nernst equation-derived formula:

$$E_{RHE} = E_{Ag/AgCl} + E^{\circ}_{Ag/AgCl} + 0.059pH - E_{cal}$$

$E_{Ag/AgCl}$ is the measured potential, $E^{\circ}_{Ag/AgCl}$ is taken to be +0.197 V, and E_{cal} is a calibration potential. The calibration potential was the voltage drop across the reference electrode and a *standard* reference electrode (always connected to the COM terminal of the voltmeter)

https://doi.org/10.1021/jacs.3c05706
J. Am. Chem. Soc. 2023, 145, 17406–17419

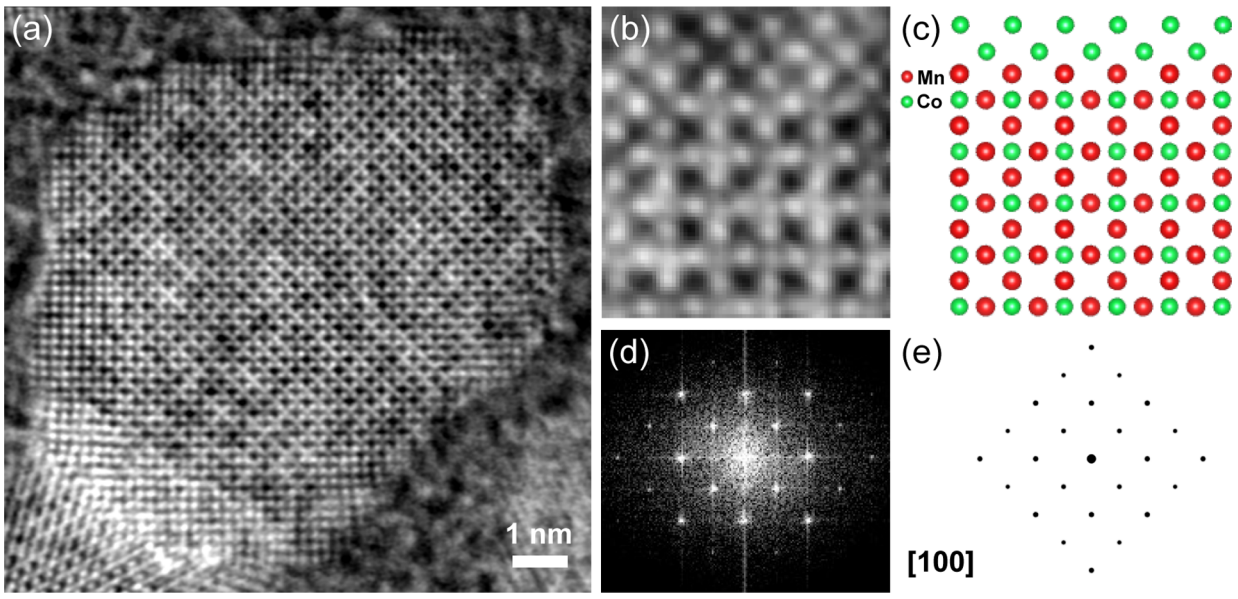

Figure 2. ABF-STEM characterization of $Co_{1.31}Mn_{1.69}O_4$ nanocrystals (CMO-03). (a) High-resolution ABF-STEM with an inverted contrast image viewed down the [100] zone. (b) Magnified ABF-STEM with an inverted contrast image viewed down the [100] zone. (c) Model of the $CoMn_2O_4$ [100] with a rock-salt CoO shell. (d) FFT taken from the center of nanocrystals in (a). (e) Kinematic electron diffraction simulation of single-crystal $CoMn_2O_4$.

not used for experiments. Voltammetric polarization curves were performed in Ar- or O_2-saturated 1 M KOH, at the reported scan and rotation rates, with the initial sweep starting in the anodic direction. To modify the working electrode with the desired catalyst composite, ~7 μL of the appropriate 5 mg/mL catalyst composite ink, using 0.25 wt % Nafion in *n*-PrOH:H_2O (3:1), was drop-cast on the glassy carbon, mounted on an inverted rotator, and allowed to dry in air at 600 rpm. The exact volume of ink applied was calculated using the composite catalyst-to-support percent, composite ink concentration, and electrode area (0.196 cm^2), with an active material (i.e., spinel oxide) target loading of 100 $\mu g/cm^2$. The modified electrode was then carefully wet with DI water prior to electrochemical testing to avoid the formation of large bubbles when submerged into the electrolyte.

RESULTS AND DISCUSSION

In a typical synthesis, a 1-to-1 ratio of $Co(acac)_2$ to $Mn(acac)_2$ was added to a round-bottom flask with amine ligand (0.1 to 0.5 M metal$(acac)_2$ in amine). After a vacuum-purge cycle with nitrogen, the flask was charged with a needle flowing dry air, and the temperature was ramped to the reaction temperature (130 to 230 °C) and held for 20 to 70 min, with the reaction finally being quenched by submersion in a water bath and cessation of the air flow. The particles were then treated with lauric acid before washing with hexane and acetone. More detailed general reaction conditions and the specifics for each sample are provided in the Experimental Section and Table S1.

TEM images of the reaction product displayed faceted spherical nanocrystals (Figure 1a, reaction CMO-01) with an average diameter of 5.8 ± 1 nm (18% dispersity) (Figure 1a, inset). HAADF-STEM imaging showed single-crystal spinel nanocrystals viewed down the [110] zone (Figure 1b). The characteristic spinel [110], [111], and [210] zone axes are also apparent from HAADF-STEM images (Figure S1). ABF-STEM images of CMO spinel nanocrystals synthesized with octylamine (Figure 2a,b) viewed down the [100] zone also show the characteristic spinel lattice. This arrangement maps exactly to models of the atomic lattice (Figure 2c), with both showing a thin region of rock salt (Figure 2b,c, upper portion). *d*-spacings were found to be 2.08 Å (220) and 1.46 Å (400) by analysis of the fast Fourier transform (FFT) of ABF-STEM images (Figure 2d) of the core of the particle, in line with the lattice spacings of bulk Co-Mn spinel oxides (PDF No.01-077-0471) and with the kinematic electron diffraction simulation of single-crystal $CoMn_2O_4$ (Figure 2e). ABF-STEM imaging also shows a very thin (1−2 lattice planes) rock-salt shell (Figure 2a). Such a shell becomes more evident after baking under vacuum (Figure S2), but it is not apparent whether the shell is a product of synthesis or due to sample processing before imaging. The PXRD peaks of a CMO-02 reaction product (Figure 1c) align well with the $CoMn_2O_4$ reference (Figure 1c, red bars, JCPDS # 01-077-0471). Debye−Scherrer analysis suggests an average crystallite size of 6.3 nm (Figure S3), which matches with the result obtained from TEM, indicating that, on average, the particles are single-domain crystals. Additionally, there is no evidence of significant amounts of the rock-salt impurity phase from the XRD (Figure 1c, purple bars, JCPDS # 00-009-0402).

XPS of the Mn 2p and Co 2p peaks of a CMO-03 synthesis suggests that the Mn cations tend to have a higher average oxidation state than Co, with most Mn cations in the 3+ oxidation state. The survey spectra indicate the presence of Co, Mn, oxygen, nitrogen, and carbon as expected (Figures S4 and S5). By peak-fitting analysis of the Mn 2p regions, a Mn^{2+}/Mn^{3+} ratio of 0.55 was found (Figure 1d, Table S2). Through a similar analysis of the Co 2p peak, a Co^{2+}/Co^{3+} ratio of 1.11 was found (Figure 1e, Table S2). The higher average oxidation state of the Mn cations in the nanocrystal product is consistent with the more electropositive nature of the Mn cation with a lower potential for the 2+/3+ redox couple compared to that of Co.[49] In our work, we utilize 2+ metal-acac precursors, but spinels necessarily have a mix of oxidation states.[1] Thus, it is necessary to oxidize 2+ cations to the higher oxidation state needed for the spinel phase. The higher average oxidation state of the Mn cations, by XPS, suggests that their oxidation in solution enables the formation of the spinel phase. Thus, we

https://doi.org/10.1021/jacs.3c05706
J. Am. Chem. Soc. 2023, 145, 17406−17419

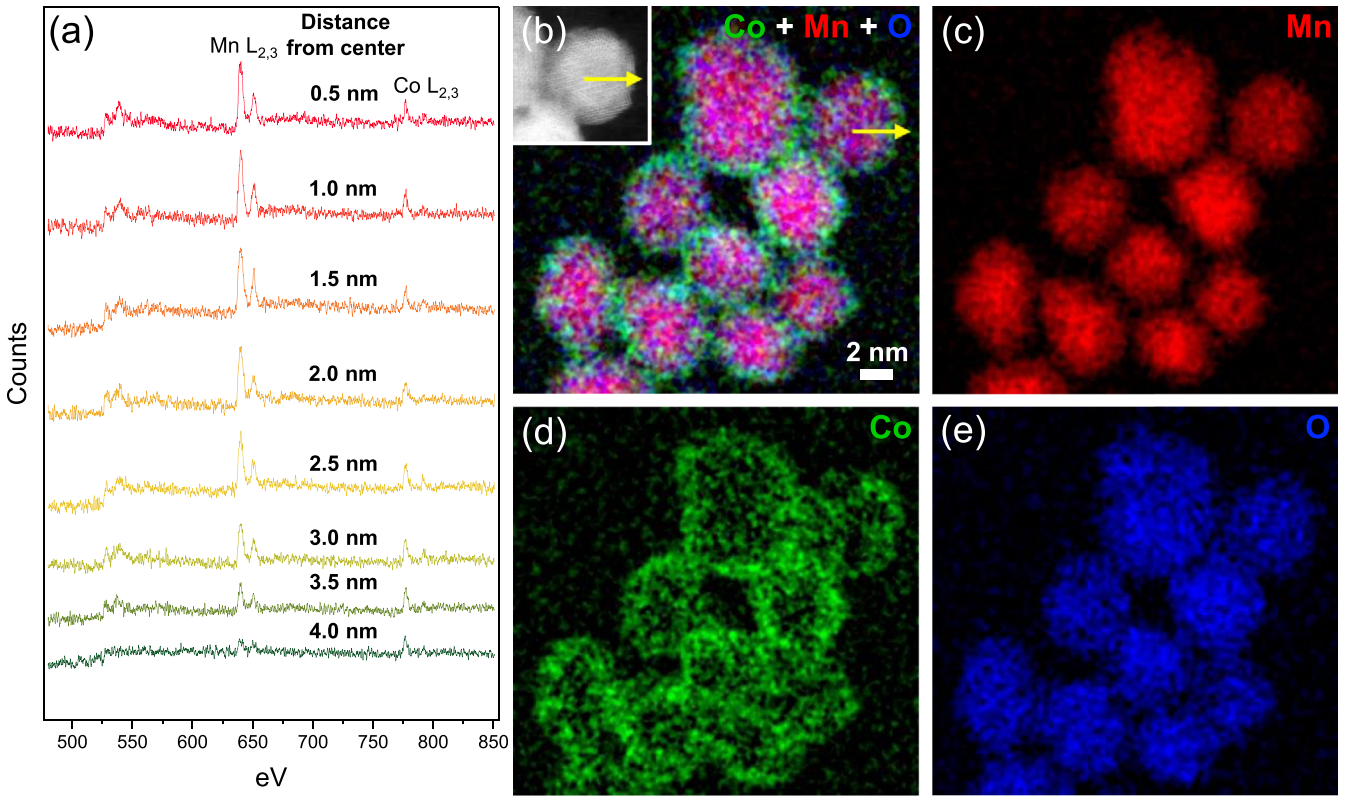

Figure 3. Characterization and investigation of the gradient core-shell structure. EELS mapping of the $Co_{1.31}Mn_{1.69}O_4$ (CMO-03) spinel nanocrystals from large-scale synthesis showing a Mn-rich core and a Co-rich shell. (a) Depth profiling spectra traversing from the core (top, red) to the shell (bottom, green) of $Co_{1.31}Mn_{1.69}O_4$ nanocrystals (CMO-03). (b) Composite map of Co, Mn, and O with the inset of HAADF image. (c) Mn Map. (d) Co map. (e) Oxygen (O) map. Scale bar 2 nm.

propose that Mn goes through oxidative decomposition, especially at lower reaction temperatures, whereas the Co precursor involves a greater contribution of the redox-neutral decomposition mechanism of metal-acac complexes in amine solvents, as suggested by Pinna et al.[44] For the $MnCo_2O_4$ system, Wei et al. found the average oxidation state of Co to be around +2.5 and the oxidation state of Mn to vary between +3.2 and +3.7 depending on the annealing temperature.[27] The through-peak fitting of XPS spectra of the work of Du et al. arrived at similar conclusions with a more-oxidized Mn, with calculated ratios of 0.13 and 3.81 for the Mn^{2+}/Mn^{3+} and Co^{2+}/Co^{3+}cations, respectively.[21] X-ray emission spectroscopy (XES) experiments of a Mn-Co-O colloidal nanocrystal supercapacitor also indicate low quantities of Co^{3+} cations and a low Mn^{2+}/Mn^{3+} ratio for the composition with 1:1 manganese to cobalt.[9]

The impact of the conversion of L-type amine ligands into organic byproducts during synthesis, and depletion during purification, is evidenced by the colloidal instability of the nanocrystals (Figure 1f, **I**–**II**). As discussed later, the amine ligand is required for $M(acac)_2$ precursor decomposition and the aerobic oxidation process that leads to the formation of the spinel phase, but simultaneously through other oxidative processes, the amines are converted to organic byproducts. Through the typical synthesis with amines and subsequent washing, nanocrystals aggregate at the bottom of the solution, indicating poor colloidal stability (Figure 1f, **I**). The addition of excess amine ligands at the end of the reaction does not increase their solubility and, in fact, surprisingly, lowers the colloidal stability of the nanocrystals (Figure 1f, **II**). We ascribe this decrease in colloidal stability to the L-type ligand-promoted displacement of Z-type ligands, induced by the additional amine, as described by Owen and co-workers and confirmed by others.[62−64] This ligand displacement removes surface metal cations bound to carboxylates (Z-type ligands), decreasing the colloidal stability of the sample by lowering the available surface site for organic ligands to bind to. Carboxylates are observed on the particle surface after synthesis (Figures 4 and S18, Table S3) due to the oxidation of the amine ligand during synthesis, similar to results seen by Calcabrini et al.[54] (in the synthesis of cerium oxide nanocrystals using a cerium nitrate precursor and OLAM). In contrast, when additional X-type ligands (e.g., lauric acid) are added at the end of the reaction, the nanocrystals have high colloidal stability after washing, without precipitates (Figure 1f, **III**). The increase in colloidal stability of the nanocrystals treated with X-type ligands can be rationalized by the ligands being bound more tightly than the native L-type amine ligands. X-type ligands may bind more tightly due to an increased electrostatic attraction between the anionic ligand and the cationic particle surface.[65−67] In summary, though we find that amine ligands and an aerobic environment are necessary during synthesis to form spinel phase nanocrystals, the addition of an X-type ligand after synthesis is necessary to ensure the colloidal stability of the nanocrystals.[67] This colloidal instability, due to the weak amine interactions, and a lack of X-type ligands may be another factor that has limited the success of colloidal spinel oxide nanocrystal syntheses.

Through tuning the cation precursor composition and reaction temperature, a range of compositions could be

https://doi.org/10.1021/jacs.3c05706
J. Am. Chem. Soc. 2023, 145, 17406−17419

realized. TEM images for a span of compositions of Co-Mn spinel oxide ranging from 0 to 56% show well-dispersed nanocrystals (Figure 1g–j). All compositions had a size dispersity below 20% and an average size between 5 and 9 nm. The ability to control the composition of these ternary oxides while maintaining single phase, small, and monodisperse particle distributions enables studying the effect(s) of cation distribution and size on the properties, without other confounding variables.

Evident in EELS mapping is a Mn-rich spinel core with a Co-rich gradient shell (Figure 3b–e). The gradient core-shell structure is corroborated by energy-dispersive X-ray spectroscopy (EDS) mapping (Figure S6), and depth profiling EELS spectra from the shell to the core of the nanocrystal (Figures 3a, S7) which shows the Mn $L_{2,3}$ peaks (~635–655 eV) steadily decreasing toward the shell of the nanoparticle, whereas the Co $L_{2,3}$ peaks (~775–795 eV) remain relatively constant throughout the particle. An EELS line scan across a CMO-03 nanocrystal taken from the characteristic Co, Mn, and O energy loss peaks showed similar Mn depletion in the particle shell (Figure S8). The Mn-rich core and Co-rich shell suggests that the Co precursor decomposes later in the synthesis, presumably at higher temperatures. The existence of the Mn-rich core combined with the limited ability to incorporate cobalt into the spinel phase (composition is limited to ~60% Co, Figure 1g–j) suggests that Mn is responsible for the formation of the spinel nuclei. The Mn-rich core and Co-rich shell is consistent with our previous reports of Co-Mn-O nanocrystal supercapacitors.[9]

D/TGA curves of precursors in OLAM (Figure S9a,b) indicate a clear difference in decomposition rate for different compositions of metal precursors, especially in a time frame that mimics typical reaction conditions. Over the course of a D/TGA experiment, the samples are run through three distinct heating stages in an air environment. In the first stage, the samples are heated from room temperature at 4 °C/min to 160 °C (Figure S9, region **I**). In the second stage, the samples are maintained at 160 °C for 30 min (Figure S9, region **II**). In the final stage, the temperature was further raised from 160 to 600 °C at 10 °C/min (Figure S9, region **III**). Three samples were run: $Co(acac)_2$ in OLAM, $Mn(acac)_2$ in OLAM, and the full synthesis precursor set (Figure S9, **green, red**, and **black plots**, respectively). The curves where manganese is present (Figure S9, **black** and **red plots**) have higher decomposition rates than the cobalt only run under standard reaction temperatures (Figure S9, **green plot**). This difference in decomposition rate further supports the earlier evidence (Figure 1d,e) that suggests that the Co precursors decompose under a different mechanism than the Mn precursor under this synthetic protocol and thus forms Mn-rich nuclei which represent the core of the nanocrystal (Figure 3).

Reaction Mechanism. To investigate the reaction mechanism, we reproduced previous syntheses and varied the purity of the precursors. Attempts to reproduce colloidal Co-Mn spinel oxides from previous work,[52] using a 1:1 cobalt to manganese molar ratio in a nitrogen atmosphere with technical grade OLAM (70%), were unsuccessful and resulted, instead, in a mixture of rock-salt and spinel oxide nanocrystals (Figure S10a). It is well known that ligand choice can affect the resulting nanocrystal phase.[68] Reactions using either low-purity or technical-grade ligands are known to have detrimental effects on colloidal nanocrystal syntheses.[65,69] In our case, using distilled OLAM (distilled over calcium hydride in order to exclude most organic impurities and water) favored the rock-salt phase impurity, being the only product obtained, for the distilled OLAM reactions (Figure S10b). We suspect that oxidized amine derivatives are present in non-distilled OLAM and that they are responsible for enabling the production of appreciable amounts of the spinel phase, even without an obvious oxidant (i.e., air) present in the system. Without the presence of oxidized amines, the solution of pure amines in a nitrogen atmosphere is quite reducing in nature and does not allow for the generation of higher oxidation state cations necessary to form the spinels. The use of 3+ or a mixture of 2+/3+ acac precursors in a nitrogen atmosphere also leads to the formation of rock salt, again, likely due to the reducing potential of the amine (or alcohol) ligand (Figures S13 and S14). From these results, we concluded that changing the precursor oxidation state will not achieve our goal of synthesizing the more highly oxidized spinel phase. Instead, based on our experience with impure OLAM, we hypothesized that using a more oxidizing environment during synthesis would enable the formation of the desired phase, and so we began carrying out the synthesis under dry air flow (Figure S10c).

The general reaction scheme for the formation of our nanocrystals (Scheme S1) describes an initial oxidative $Mn(acac)_2$ decomposition to form metal oxo complexes that aggregate to create nuclei for a Mn-rich core. Then, at higher temperatures, $Co(acac)_2$ decomposes at a faster rate than the $Mn(acac)_2$ and forms CMO layers on the nanocrystals. Thus, there is an inherent composition gradient of the cations in the resulting nanocrystals. Control studies show that amines are necessary for the oxidative decomposition mechanism to occur and form the pure spinel phase. Reactions with no amines present resulted in mixed phase oxides or in no solid product (Figure S11a,b). The amine reacts with molecular oxygen to produce a variety of oxidized amine derivatives (discussed later in Figure 4) and likely acts as a redox mediator for the oxidation of the metal-acac precursors by molecular oxygen. When $Co(acac)_2$ is the only precursor present, the decomposition proceeds through an alternative mechanism, likely the non-oxidative route described by Pinna et al.,[44] shown by formation of the rock-salt oxide (Figure S12b). In contrast, the Mn-only synthesis produces fully spinel nanocrystals (Figure S12a). The fact that Co still has a mixture of oxidation states in the final nanocrystal product of a normal CMO synthesis, confirmed by XPS (Figure 1e), suggests that cobalt undergoes partial oxidation when adsorbing to the nanocrystal, which is different from the non-oxidative route it undergoes when cobalt is the sole metal (Figure S12b). The fact that Mn forms the core of the nanocrystal and decomposes at higher rates than the Co precursor at low temperatures (Figures 3 and S9) is consistent with this hypothesis. Importantly, the oxidative decomposition of the Mn precursor to preferentially form spinel oxide is surprising since a variety of manganese oxide phases are relatively stable[70] (MnO, Mn_3O_4, Mn_2O_3, MnO_2, etc.). This high selectivity for the spinel phase suggests that this synthesis methodology is applicable to a variety of Mn-based spinels. In fact, this selectivity is so dramatic that when a typical precursor mixture (1:1 cobalt to manganese acetylacetonate precursor in alkylamine) was injected with an aqueous solution of 30% hydrogen peroxide at 100 °C under a nitrogen atmosphere, almost pure Mn spinel (90% by ICP) was formed with no phase impurity (Figure S11d). This result is interesting

https://doi.org/10.1021/jacs.3c05706
J. Am. Chem. Soc. 2023, 145, 17406–17419

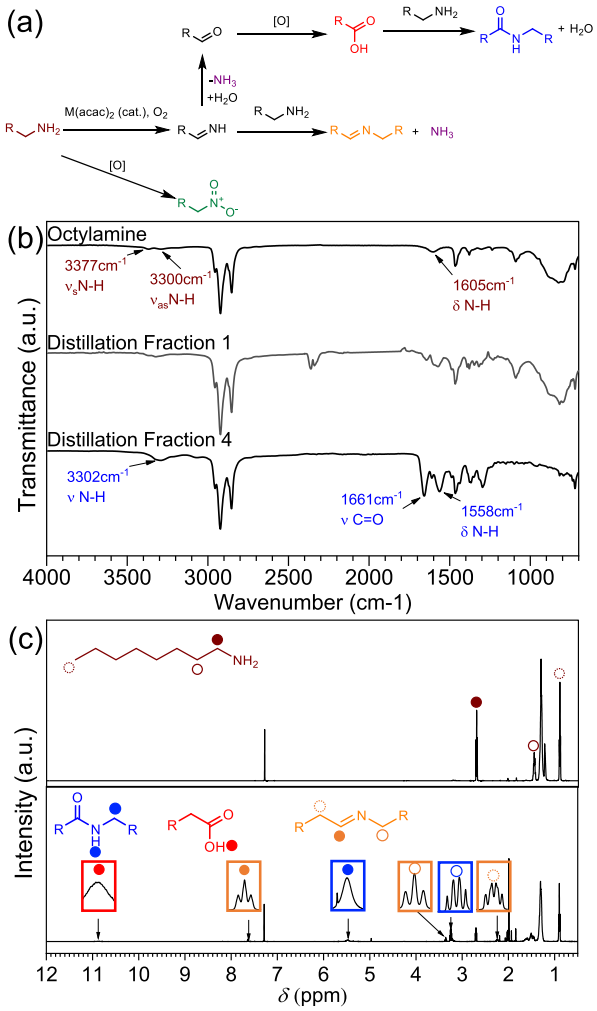

Figure 4. Organic byproduct generation mechanism. (a) General scheme for the organic byproduct generation mechanism, with observed byproducts in color. (b) FTIR of octylamine and distillation of reaction solution CMO-09, with peaks of observed compounds assigned, see Table S3 for vibrational assignments. (c) NMR spectra of distillation fractions 1 and 4 from the same reaction, with peaks assigned to hydrogens adjacent to circles in inset.

because hydrogen peroxide is likely a byproduct of the dehydrogenative imine formation from the amine ligand and molecular oxygen as we show later in this work. This may help explain the Mn-core formation due to preferential decomposition in the presence of peroxyl intermediates during ligand decomposition at lower temperature.

Organic Side Products. The amine ligands decompose throughout the course of the nanocrystal synthesis, forming organic byproducts (Figure 4, Table S3). It should be noted that there is no line broadening typical of NMR in nanocrystal systems and is even more typical in complexes containing paramagnetic nuclei like in this synthesis. The reason that no line broadening is observed is because we distill the final reaction solution to rid the NMR samples of nanocrystals or any paramagnetic precursors/intermediates while also concentrating the higher molecular weight byproducts, both of which aid in making accurate NMR assignments. The prominent amide byproduct (Figure 4, **blue**), found in both the NMR and FTIR[71] of distillation fraction 4, is formed first through the 2-electron oxidation of the amine to imine.[72−76] Hydrolysis (via water produced by the reduction of molecular oxygen) could then provide the corresponding aldehyde, which further oxidizes, under the aerobic reaction conditions, to produce a carboxylic acid (Figure 4a,c, **bright red**).[54] The carboxylic acid then undergoes condensation with an amine to form the observed amide. Alternatively, the imine (or aldehyde) could condense with another amine to produce the observed secondary imine product (Figure 4a,c, **orange**).[53,54,76] Both mechanisms would also generate appreciable amounts of ammonia (Figure 4a, **dark purple**), and this is evidenced by positive ammonia tests from a vessel containing DI water through which the reaction effluent gas was bubbled (Figure S19). Also, appreciable amounts of nitro-octane (Figure 4a, **green**) are observed on the particle surface by FTIR (Figure S18, Table S3, **N−O stretch**),[77,78] which we believe are derived from an alternative amine oxidation mechanism.[79,80]

These organic byproducts, especially the imine and amide, are difficult to purify from the resultant reaction mixture because they can precipitate upon antisolvent addition. In a typical synthesis with OLAM as the capping ligand (Figures 5a, S20a), the workup required more than four washes to produce a dry product, often leading to aggregated particles. When only one wash was used, high organic loading (∼50 wt %) was observed by TGA (Figure S21), highlighting the difficultly in removing high-molecular-weight organic byproducts during typical solvent-antisolvent washes. This difficulty in purification is ascribed to the long-chain (amide and imine) byproducts being sufficiently hydrophobic to result in their precipitation, along with the nanocrystal product, upon antisolvent addition. Thus, the typical solvent-antisolvent strategy of nanocrystal purification was inefficient in isolating particles with low organic loading. This effect is exacerbated when longer chain amine ligands, like those typical of colloidal nanocrystal syntheses, are used (such as OLAM) because the longer alkyl chain causes the resultant amide or imine byproducts to be >500 Da of almost completely aliphatic hydrocarbon, increasing the propensity of the byproducts to precipitate during washes. The coprecipitation of nanocrystals and organic byproducts limits the purity of the nanocrystal product while providing little aid in colloidal stability. De Roo and co-workers[53,54] have also observed the formation of high-molecular-weight organic byproducts from nanocrystal syntheses containing amines, specifically the amide and imine byproducts which are especially difficult to purify during solvent/antisolvent washes. We hypothesized that using an amine with a shorter alkyl chain would allow for more facile purification of nanocrystals (Figures 5b and S20b) due to the lower hydrophobicity of its organic byproducts. In order to test this theory, we ran TGA on nanocrystal products from two different reactions, one using OLAM (Figure S22a) and another using the shorter-chain octylamine (Figure S22b), and then cleaned the products using three different purification strategies (no excess post-synthetic ligand added, addition of the corresponding amine, or addition of lauric acid: Figure S22a,b, **blue, green, red**, respectively). Based on the location of the TGA profile plateaus above 200 °C, all products from the octylamine synthesis had lower organic loadings than those from the OLAM synthesis, for all purification strategies (Figure S22a,b).

In addition to the excess organic byproduct with longer amine chains, the native amine passivation provided poor solubility of the nanocrystals. Due to the weakness of the coordinate−covalent bond of the amine to the surface of the

https://doi.org/10.1021/jacs.3c05706
J. Am. Chem. Soc. 2023, 145, 17406−17419

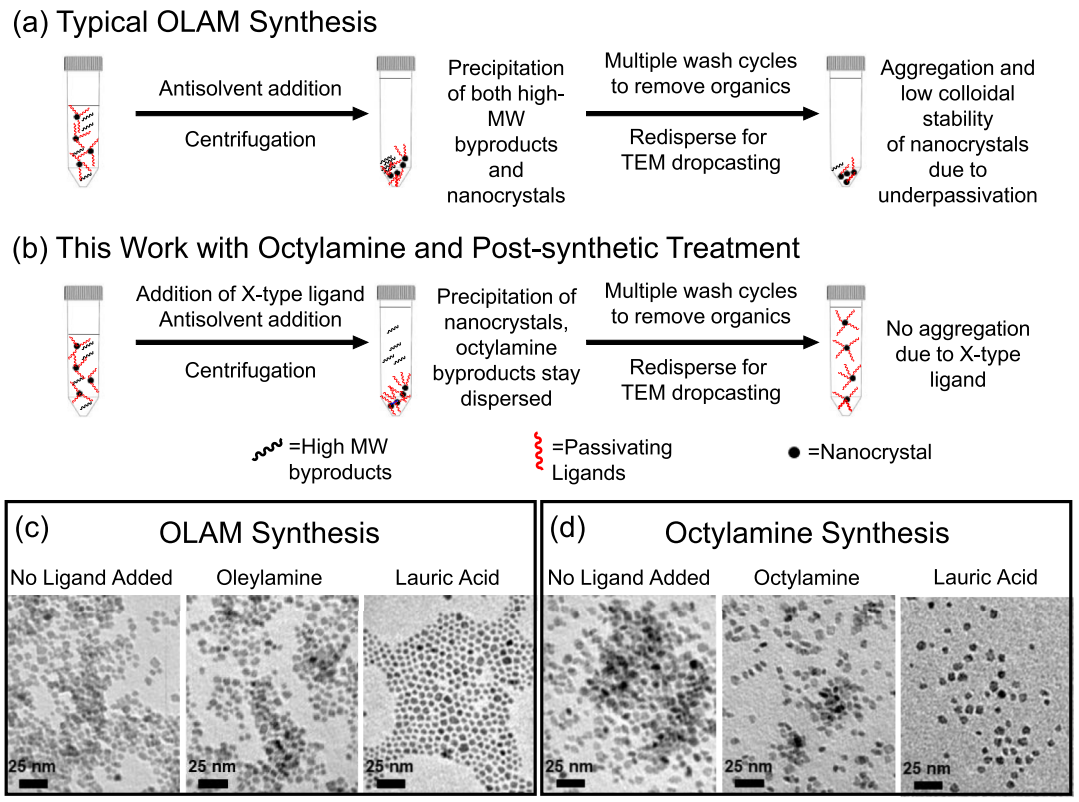

Figure 5. Purification strategy: (a) proposed mechanism for the product of the wash strategy for the OLAM reaction. (b) Proposed mechanism for the product of the wash strategy for the octylamine reaction with lauric acid post-synthetic treatment. (c) TEM images of final nanocrystal products of the OLAM reaction after post-synthetic treatments. (d) TEM images of final nanoparticle products of the octylamine reaction after post-synthetic treatments. Reaction conditions and post-synthetic treatments listed in Table S1.

particle, washing the nanocrystals resulted in under-passivated surfaces[81] that tended to aggregate regardless of the amine chain length (Figure 5c,d, **no ligand added**). This lack of stability is disadvantageous for processability and applications. There is the possibility that under-passivation could be caused by depletion of the amine ligand during synthesis by transformation into even more weakly coordinating species like amides or imines. To demonstrate that the aggregation was due to colloidal instability during washes, we post-synthetically treated the nanocrystals with an additional amine ligand (see Methods) (Figure 5c,d, **OLAM** and **octylamine**). However, the TEM images show almost completely aggregated products in both cases, suggesting that the amine ligand is lost in the wash. We hypothesized that a stronger binding X-type ligand such as a carboxylic acid may be less likely to be removed during washes and may allow for multiple rounds of solvent-antisolvent washes without degrading the colloidal stability. The tendency for X-type ligands to bind more tightly than L-type ligands has been reported in the literature[65,67,69,81] and can be ascribed to the electrostatic attraction between the cationic metal sites that typically dominate semiconductor nanocrystal surfaces[65,82,83] and the anionic carboxylate ligand. As shown in the TEM images (Figure 5c,d, **lauric acid**), the particles that were treated with a small amount of lauric acid at the end of the synthesis freely dispersed in solution and no aggregates were observed on the TEM grid. This result agrees with the results shown in the optical photo of these colloidal dispersions in Figure 1f. The TGA profiles of the final products from the lauric acid treatment (Figure S22a,b, **red curves**) show higher organic loading than the other profiles which were not treated with an X-type ligand. This is consistent with the hypothesis that X-type ligands are not washed away to the same degree as L-type ligands. This strategy of using shorter chain ligands during synthesis and a post-synthetic treatment with X-type ligands (Figure 5b) is ideal for generating colloidally stable nanocrystals with relatively low organic byproducts.

To probe the effect of the high-molecular-weight organic byproducts on ORR electrocatalysis, we synthesized nanocrystals at both 130 and 160 °C in OLAM and at 160 °C in octylamine (CMO-10, CMO-11, and CMO-03, respectively). After purification, the nanocrystals were combined with Ketjenblack (KB) with a target nanocrystal loading of 65 wt % and annealed at 175 °C to remove the organics. Each composite from this process was then analyzed by D/TGA (see Experimental Section for details) (Figure S23a,b). Both OLAM composites exhibited higher carbon/organic loadings (Figure S23a, **blue and red**) than the octylamine composite (Figure S23a, **green**). Interestingly, the carbon decomposition in the 160 °C OLAM synthesis is shifted to quite higher temperatures and has a much slower decomposition rate for carbon-containing matter than the other two composites (Figure S23a,b, **red**). This result may be due to the difficulty of removing large amounts of high-MW organic byproducts from the carbon in the composite or reactions between the OLAM and its byproducts and the carbon support.

Electrochemical Characterization. Electrochemical characterization was performed on the KB composites after depositing a film of the composite in an alcohol-water solution onto a rotating disk electrode (RDE) using Nafion as the

https://doi.org/10.1021/jacs.3c05706
J. Am. Chem. Soc. 2023, 145, 17406−17419

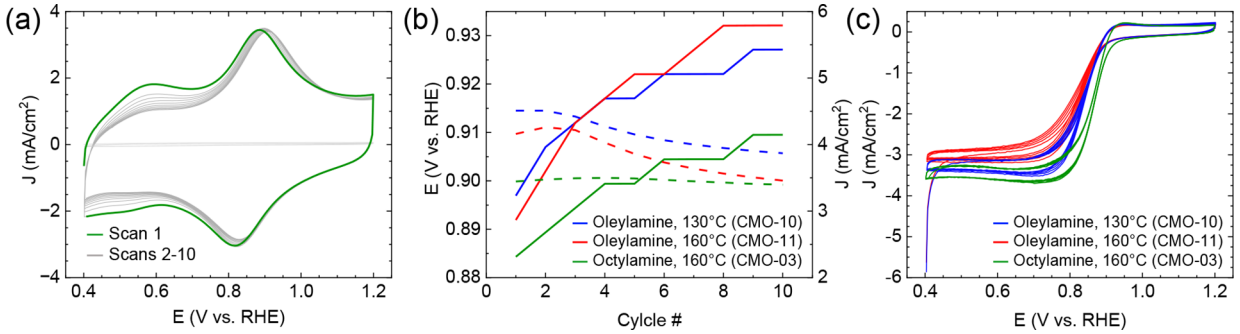

Figure 6. Basic electrochemical characterization of CMO nanocrystal–KB composites: (a) cyclic voltammogram of the CMO-03/KB composite in 1.0 M KOH and an argon atmosphere, 10 cycles. (b) Change in oxidation peak current density (J, dashed lines) and position (E, solid lines) for CMO/KB composites synthesized under various conditions. (c) ORR performed with CMO/KB composites synthesized under various conditions.

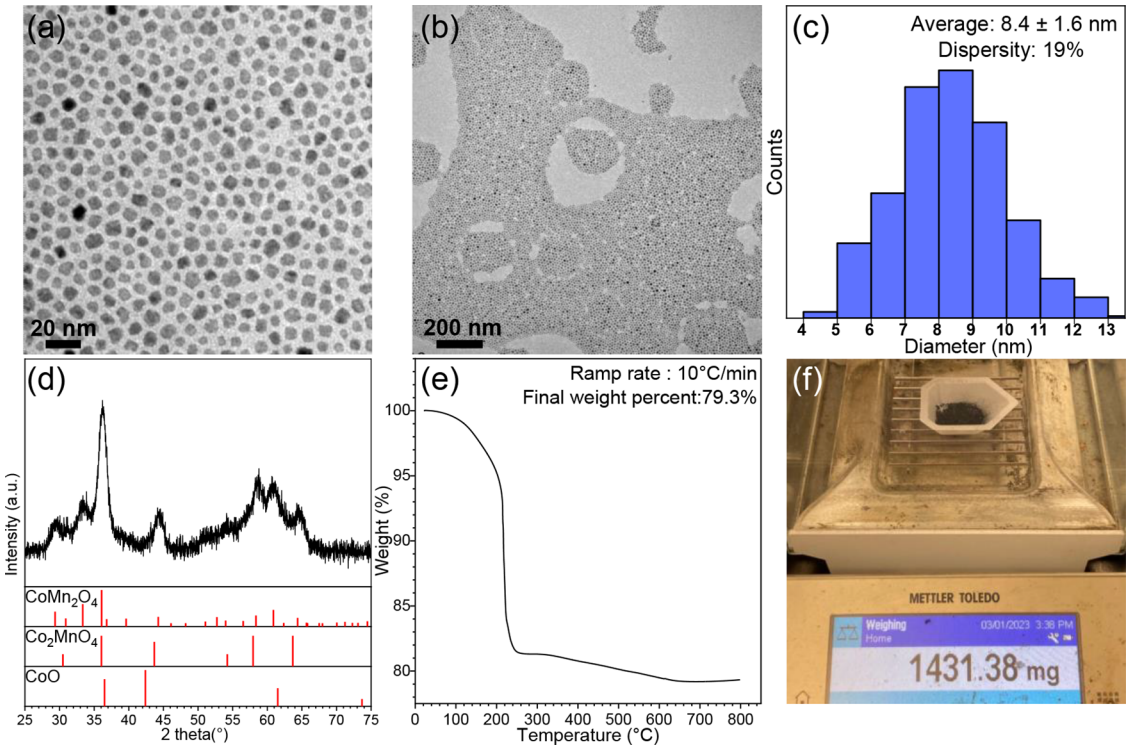

Figure 7. Low-res TEM, particle size distribution, XRD, TGA, and picture of $Co_{1.31}Mn_{1.69}O_4$ spinel oxide nanocrystal large-scale synthesis (CMO-03). (a, b) TEM images of nanocrystals. Images show the superlattice of small particles even up to the micron scale. (c) Particle size distribution of nanocrystals. (d) PXRD result of nanocrystals. The result matches the reference diffraction pattern of $CoMn_2O_4$. The $CoMn_2O_4$, Co_2MnO_4, and CoO JCPDS reference numbers are 01-077-0471, 00-002-1061, and 00-009-0402, respectively. (e) TGA result of $Co_{1.31}Mn_{1.69}O_4$ shows ~20% of the organic ligand on the surface of nanoparticles. (f) Picture of nanoparticle powder being weighed for yield. After accounting for the organic ligands, the yield is found to be 1.135 g of the $Co_{1.31}Mn_{1.69}O_4$ spinel nanocrystal.

binder (see Experimental Section for details). The cyclic voltammograms of the composites in Ar-saturated 1 M KOH showed a decrease in current density and a shift in the formal potential of the redox couple for all samples as a function of cycling. However, the shift in potential and decay in current density per cycle was least apparent for the octylamine sample (Figures 6b, S24, and S25). The RDE cycles (0.4 to 1.2 V vs RHE) performed on the composites in O_2-saturated 1 M KOH (Figures 6c, S24, and S25) followed a similar behavior as the Ar-saturated 1 M KOH cyclic voltammograms for the OLAM syntheses (Figure 6b, **red** and **blue**) with the most unstable behavior being exhibited by the higher temperature OLAM sample (Figure 6b,c, **red**). Comparatively, the octylamine composite electrochemistry showed little to no change while catalyzing the ORR (Figure 6c, **green**), and the final cycle of the octylamine composite outperformed the 130 and 160 °C OLAM synthesis in terms of the half-wave potential ($E_{1/2}$) by 30 and 50 mV, respectively. Of the three Co-Mn composites, the octylamine synthesis-based composite also showed the highest ORR diffusion-limited current density (j_l) (Figure 6c) and an ORR $E_{1/2}$ of 0.87 V vs RHE in 1.0 M KOH at 1600 rpm, which approaches the highest ORR activity reported for this material of 0.89 V vs RHE.[16] The more stable $E_{1/2}$ and j_l for the octylamine synthesis-based composite, compared to the OLAM counterpart, is likely due to multiple factors. One possibility is that the higher molecular weight organics, left in the high-temperature OLAM sample, increase ohmic losses which worsen as the organics react at the electrode surface as a

https://doi.org/10.1021/jacs.3c05706
J. Am. Chem. Soc. 2023, 145, 17406–17419

function of cycling. Another possibility is that the larger hydrodynamic radii of the OLAM nanocrystals (due to longer alkyl chain length) weaken the catalyst−carbon support interaction during composite synthesis. Yet another possibility is that the remaining organics left after annealing aid in the dissolution of surface cations since it is well known that counteranions can play a major role in dissolution kinetics,[84,85] which could alter the ORR activity. Overall, it is clear that using a shorter chain amine, as the initial ligand, lowers the molecular weight of the resulting organic byproducts such that they can be removed using a mild (175 °C) thermal annealing, whereas high-molecular-weight ligands, like OLAM, which are typically used in colloidal synthesis, tend to be deleterious to electrochemical applications due to their undesirable adsorbing byproducts.

Generality of Reaction Mechanism and Scale-Up. To further demonstrate the generality of this mechanism, we ran the synthesis with a variety of amine ligands (Figure S26, **OLAM, octylamine, dodecylamine, benzylamine, and dioctylamine**). All particles, except the dioctylamine sample, which had a much smaller particle size, displayed faceted spherical to cubic morphologies with particle sizes averaging 5−10 nm. Furthermore, we applied this synthesis to a variety of manganate spinels with a 1:2 ratio of other metal-acac to $Mn(acac)_2$ (Figure S27). Nickel, zinc, iron, and copper were all effectively incorporated into the spinel lattice according to ICP (Table S1). All samples were small and relatively of low dispersity, with all PXRD patterns confirming the spinel phase. While iron and zinc both appeared to be close to the desired composition of the synthesis, copper and nickel both incorporate into the final product to a lower extent. Finally, we show that this synthesis is reproducible and highly scalable; we scaled up the reaction by 9× and achieved gram-scale quantities of the inorganic product, as confirmed by TGA. TGA provides the percentage of the final product mass that is inorganic nanocrystal from that of the ligand or other organic byproducts. At 1.43 g of total product, containing 1.14 g of the $Co_{1.31}Mn_{1.69}O_4$ spinel nanocrystal (54% of theoretical), we were able to maintain small and low dispersity and particle size (Figure 7), showing the highly scalable nature of our methodology. We then repeated this procedure and found similar results (Figure S28), demonstrating the reproducibility of this gram-scale synthesis.

CONCLUSIONS

In this work, we have developed a general, low-cost, scalable synthetic methodology for small, low-dispersity, colloidally stable manganate nanocrystals. The synthesis is highly selective for the spinel phase with a wide range of compositions and particle size control. We investigated the mechanistic origins of the gradient core-shell structure inherent to the nanocrystal product and determined that it arose from the Mn precursor undergoing oxidative degradation at lower reaction temperatures. We showed the transformation of the amine ligands during synthesis and its effects on particle surface chemistry and application performance. Our methodology, using short-chain amine ligands during synthesis, reduces organic contamination and purification time, while post-synthetically modifying the particles with an X-type ligand prevents particle aggregation. Finally, we show the reproducible gram-scale synthesis of these particles while maintaining particle size, dispersity, and crystal structure, along with the generality of this method to many Mn-based spinels and amine ligands. This work opens the door to more fundamental studies correlating application performance (e.g., electrocatalytic ORR) to fundamental properties of the manganate spinel nanocrystals, free from confounding variables such as organic contamination and nanocrystal aggregation. The high scalability and low cost of this method, in comparison to other syntheses, combined with the high processability of colloidal nanoparticles, also hold promise for the real-world applications of these nanocrystals in fuel cell, electrolyzer, or supercapacitor applications.

ASSOCIATED CONTENT

Supporting Information

The Supporting Information is available free of charge at https://pubs.acs.org/doi/10.1021/jacs.3c05706.

Additional information on reaction condition specifics, Debye−Scherrer analysis, XPS data, EDS data, D/TGA, control studies, NMR data, FTIR data, schemes, electrochemical characterization, and characterization of syntheses using other amines and other Mn-based spinels (PDF)

AUTHOR INFORMATION

Corresponding Author

Richard D. Robinson − *Department of Materials Science and Engineering and Kavli Institute at Cornell for Nanoscale Science, Cornell University, Ithaca, New York 14853, United States;* orcid.org/0000-0002-0385-2925; Email: rdr82@cornell.edu

Authors

Jonathan L. Rowell − *Department of Chemistry and Chemical Biology, Cornell University, Ithaca, New York 14853, United States;* orcid.org/0000-0002-2959-8638

Yafu Jia − *Department of Materials Science and Engineering, Cornell University, Ithaca, New York 14853, United States*

Zixiao Shi − *Department of Chemistry and Chemical Biology, Cornell University, Ithaca, New York 14853, United States*

Andrés Molina Villarino − *Department of Chemistry and Chemical Biology, Cornell University, Ithaca, New York 14853, United States;* orcid.org/0000-0003-3272-5156

Minsoo Kang − *Department of Materials Science and Engineering, Cornell University, Ithaca, New York 14853, United States*

Dasol Yoon − *Department of Materials Science and Engineering, Cornell University, Ithaca, New York 14853, United States;* orcid.org/0000-0003-2284-7010

Kevin Zhijian Jiang − *Department of Materials Science and Engineering, Cornell University, Ithaca, New York 14853, United States*

Héctor D. Abruña − *Department of Chemistry and Chemical Biology, Cornell University, Ithaca, New York 14853, United States;* orcid.org/0000-0002-3948-356X

David A. Muller − *School of Applied and Engineering Physics and Kavli Institute at Cornell for Nanoscale Science, Cornell University, Ithaca, New York 14853, United States*

Complete contact information is available at: https://pubs.acs.org/10.1021/jacs.3c05706

Author Contributions

All authors have revised the final version of the manuscript.

Notes

The authors declare no competing financial interest.

■ ACKNOWLEDGMENTS

Research primarily supported as part of the Center for Alkaline Based Energy Solutions (CABES), an Energy Frontier Research Center funded by the U.S. Department of Energy (DOE), Office of Science, Basic Energy Sciences (BES), under Award # DE-SC0019445. This work was supported in part by the National Science Foundation (NSF) under Award No. DMR-1809429. This work also made use of the Cornell Center for Materials Research Shared Facilities which are supported through the NSF MRSEC program (DMR-1719875). The FEI Titan Themis 300 was acquired through NSF-MRI-1429155, with additional support from the Cornell University, the Weill Institute, and the Kavli Institute at Cornell. The Thermo Fisher Spectra 300 X-CFEG was acquired with support from PARADIM, an NSF MIP (DMR-2039380), and Cornell University. We would like to thank Tatyana Dokuchayeva from Cornell Nutrient Analysis Laboratories for helping us with ICP-AES measurements. A.M.V. acknowledges support by the NSF Graduate Research Fellowship Program (GRFP) grant DGE-1650441 and DGE-2139899 and the Cornell Dean's Excellence Scholarship.

■ REFERENCES

(1) Zhao, Q.; Yan, Z.; Chen, C.; Chen, J. Spinels: Controlled Preparation, Oxygen Reduction/Evolution Reaction Application, and Beyond. *Chem. Rev.* **2017**, *117*, 10121−10211.

(2) Lee, N.; Hyeon, T. Designed Synthesis of Uniformly Sized Iron Oxide Nanoparticles for Efficient Magnetic Resonance Imaging Contrast Agents. *Chem. Soc. Rev.* **2012**, *41*, 2575−2589.

(3) Katzbaer, R. R.; Dos Santos Vieira, F. M.; Dabo, I.; Mao, Z.; Schaak, R. E. Band Gap Narrowing in a High-Entropy Spinel Oxide Semiconductor for Enhanced Oxygen Evolution Catalysis. *J. Am. Chem. Soc.* **2023**, *145*, 6753−6761.

(4) Padmanathan, N.; Selladurai, S. Mesoporous $MnCo_2O_4$ Spinel Oxide Nanostructure Synthesized by Solvothermal Technique for Supercapacitor. *Ionics* **2014**, *20*, 479−487.

(5) Gonçalves, J. M.; Silva, M. N. T.; Naik, K. K.; Martins, P. R.; Rocha, D. P.; Nossol, E.; Munoz, R. A. A.; Angnes, L.; Rout, C. S. Multifunctional Spinel $MnCo_2O_4$ Based Materials for Energy Storage and Conversion:A Review on Emerging Trends, Recent Developments and uture Perspectives. *J. Mater. Chem. A* **2021**, *9*, 3095−3124.

(6) Perera, S. D.; Ding, X.; Bhargava, A.; Hovden, R.; Nelson, A.; Kourkoutis, L. F.; Robinson, R. D. Enhanced Supercapacitor Performance for Equal Co−Mn Stoichiometry in Colloidal $Co_{3-x}Mn_xO_4$ Nanoparticles in Additive-Free Electrodes. *Chem. Mater.* **2015**, *27*, 7861−7873.

(7) Sahoo, S.; Naik, K. K.; Rout, C. S. Electrodeposition of Spinel $MnCo_2O_4$ Nanosheets for Supercapacitor Applications. *Nanotechnology* **2015**, *26*, No. 455401.

(8) Sun, C.; Yang, J.; Dai, Z.; Wang, X.; Zhang, Y.; Li, L.; Chen, P.; Huang, W.; Dong, X. Nanowires Assembled from $MnCo_2O_4$@C Nanoparticles for Water Splitting and All-Solid-State Supercapacitor. *Nano Res.* **2016**, *9*, 1300−1309.

(9) Bhargava, A.; Chen, C. Y.; Dhaka, K.; Yao, Y.; Nelson, A.; Finkelstein, K. D.; Pollock, C. J.; Caspary Toroker, M.; Robinson, R. D. Mn Cations Control Electronic Transport in Spinel $Co_xMn_{3-x}O_4$ Nanoparticles. *Chem. Mater.* **2019**, *31*, 4228−4233.

(10) Kim, D. K.; Muralidharan, P.; Lee, H. W.; Ruffo, R.; Yang, Y.; Chan, C. K.; Peng, H.; Huggins, R. A.; Cui, Y. Spinel $LiMn_2O_4$ Nanorods as Lithium Ion Battery Cathodes. *Nano Lett.* **2008**, *8*, 3948−3952.

(11) Qiao, R.; Wang, Y.; Olalde-Velasco, P.; Li, H.; Hu, Y.-S.; Yang, W. Direct Evidence of Gradient Mn(II) Evolution at Charged States in $LiNi_{0.5}Mn_{1.5}O_4$ Electrodes with Capacity Fading. *J. Power Sources* **2015**, *273*, 1120−1126.

(12) Cheng, F.; Wang, H.; Zhu, Z.; Wang, Y.; Zhang, T.; Tao, Z.; Chen, J. Porous $LiMn_2O_4$ Nanorods with Durable High-Rate Capability for Rechargeable Li-ion Batteries. *Energy Environ. Sci.* **2011**, *4*, 3668−3675.

(13) Zhang, G.; Xia, B. Y.; Xiao, C.; Yu, L.; Wang, X.; Xie, Y.; Lou, X. W. D. General Formation of Complex Tubular Nanostructures of Metal Oxides for the Oxygen Reduction Reaction and Lithium-ion Batteries. *Angew. Chem., Int. Ed.* **2013**, *52*, 8643−8647. (acccessed 2023/01/23)

(14) Yu, X.; Zhang, C.; Luo, Z.; Zhang, T.; Liu, J.; Li, J.; Zuo, Y.; Biendicho, J. J.; Llorca, J.; Arbiol, J.; Morante, J. R.; Cabot, A. A Low Temperature Solid State Reaction to Produce Hollow $Mn_xFe_{3-x}O_4$ Nanoparticles as Anode for Lithium-ion Batteries. *Nano Energy* **2019**, *66*, No. 104199.

(15) Yang, Y.; Peng, H.; Xiong, Y.; Li, Q.; Lu, J.; Xiao, L.; DiSalvo, F. J.; Zhuang, L.; Abruña, H. D. High-Loading Composition-Tolerant Co−Mn Spinel Oxides with Performance beyond 1 W/cm^2 in Alkaline Polymer Electrolyte Fuel Cells. *ACS Energy Lett.* **2019**, *4*, 1251−1257.

(16) Yang, Y.; Xiong, Y.; Holtz, M. E.; Feng, X.; Zeng, R.; Chen, G.; DiSalvo, F. J.; Muller, D. A.; Abruna, H. D. Octahedral Spinel Electrocatalysts for Alkaline Fuel Cells. *Proc. Natl. Acad. Sci. U. S. A.* **2019**, *116*, 24425−24432.

(17) Wang, Y.; Yang, Y.; Jia, S.; Wang, X.; Lyu, K.; Peng, Y.; Zheng, H.; Wei, X.; Ren, H.; Xiao, L.; Wang, J.; Muller, D. A.; Abruna, H. D.; Hwang, B. J.; Lu, J.; Zhuang, L. Synergistic Mn-Co Catalyst Outperforms Pt on High-rate Oxygen Reduction for Alkaline Polymer Electrolyte Fuel Cells. *Nat. Commun.* **2019**, *10*, 1506.

(18) Yan, X.; Jia, Y.; Chen, J.; Zhu, Z.; Yao, X. Defective-Activated-Carbon-Supported Mn-Co Nanoparticles as a Highly Efficient Electrocatalyst for Oxygen Reduction. *Adv. Mater.* **2016**, *28*, 8771−8778.

(19) Menezes, P. W.; Indra, A.; Sahraie, N. R.; Bergmann, A.; Strasser, P.; Driess, M. Cobalt-manganese-Based Spinels as Multifunctional Materials that Unify Catalytic Water Oxidation and Oxygen Reduction Reactions. *ChemSusChem* **2015**, *8*, 164−171.

(20) Cheng, F.; Shen, J.; Peng, B.; Pan, Y.; Tao, Z.; Chen, J. Rapid Room-Temperature Synthesis of Nanocrystalline Spinels as Oxygen Reduction and Evolution Electrocatalysts. *Nat. Chem.* **2011**, *3*, 79−84.

(21) Du, J.; Chen, C.; Cheng, F.; Chen, J. Rapid Synthesis and Efficient Electrocatalytic Oxygen Reduction/Evolution Reaction of $CoMn_2O_4$ Nanodots Supported on Graphene. *Inorg. Chem.* **2015**, *54*, 5467−5474.

(22) Fu, G.; Liu, Z.; Zhang, J.; Wu, J.; Xu, L.; Sun, D.; Zhang, J.; Tang, Y.; Chen, P. Spinel $MnCo_2O_4$ Nanoparticles Cross-linked with wo-dimensional Porous Carbon Nanosheets as a High-efficiency Oxygen Reduction Electrocatalyst. *Nano Res.* **2016**, *9*, 2110−2122.

(23) Kim, J.; Ko, W.; Yoo, J. M.; Paidi, V. K.; Jang, H. Y.; Shepit, M.; Lee, J.; Chang, H.; Lee, H. S.; Jo, J.; Kim, B. H.; Cho, S. P.; van Lierop, J.; Kim, D.; Lee, K. S.; Back, S.; Sung, Y. E.; Hyeon, T. Structural Insights into Multi-Metal Spinel Oxide Nanoparticles for Boosting Oxygen Reduction Electrocatalysis. *Adv. Mater.* **2022**, *34*, No. e2107868.

(24) Lee, E.; Jang, J.-H.; Kwon, Y.-U. Composition Effects of Spinel Mn_xCo+O_4 Nanoparticles on their Electrocatalytic Properties in Oxygen Reduction Reaction in Alkaline Media. *J. Power Sources* **2015**, *273*, 735−741.

(25) Liang, Y.; Wang, H.; Zhou, J.; Li, Y.; Wang, J.; Regier, T.; Dai, H. Covalent Hybrid of Spinel Manganese-cobalt Oxide and Graphene as Advanced Oxygen Reduction Electrocatalysts. *J. Am. Chem. Soc.* **2012**, *134*, 3517−3523.

(26) Li, C.; Han, X.; Cheng, F.; Hu, Y.; Chen, C.; Chen, J. Phase and Composition Controllable Synthesis of Cobalt Manganese Spinel Nanoparticles Towards Efficient Oxygen Electrocatalysis. *Nat. Commun.* **2015**, *6*, 7345.

(27) Wei, C.; Feng, Z.; Scherer, G. G.; Barber, J.; Shao-Horn, Y.; Xu, Z. J. Cations in Octahedral Sites: A Descriptor for Oxygen Electrocatalysis on Transition-Metal Spinels. *Adv. Mater.* **2017**, *29*, No. 1606800.

https://doi.org/10.1021/jacs.3c05706
J. Am. Chem. Soc. 2023, 145, 17406−17419

(28) Gliech, M.; Bergmann, A.; Spöri, C.; Strasser, P. Synthesis−structure Correlations of Manganese−cobalt Mixed Metal Oxide Nanoparticles. *J. Energy Chem.* **2016**, *25*, 278−281.
(29) Li, A.; Kong, S.; Guo, C.; Ooka, H.; Adachi, K.; Hashizume, D.; Jiang, Q.; Han, H.; Xiao, J.; Nakamura, R. Enhancing the Stability of Cobalt Spinel Oxide Towards Sustainable Oxygen Evolution in Acid. *Nat. Catal.* **2022**, *5*, 109−118.
(30) Ma, T. Y.; Dai, S.; Jaroniec, M.; Qiao, S. Z. Synthesis of Highly Active and Stable Spinel-type Oxygen Evolution Electrocatalysts by a Rapid Inorganic Self-templating Method. *Chemistry* **2014**, *20*, 12669−12676.
(31) Hirai, S.; Yagi, S.; Seno, A.; Fujioka, M.; Ohno, T.; Matsuda, T. Enhancement of the oxygen evolution reaction in Mn^{3+}-based electrocatalysts: correlation between Jahn−Teller distortion and catalytic activity. *RSC Adv.* **2016**, *6*, 2019−2023.
(32) Yang, Y.; Peltier, C. R.; Zeng, R.; Schimmenti, R.; Li, Q.; Huang, X.; Yan, Z.; Potsi, G.; Selhorst, R.; Lu, X.; Xu, W.; Tader, M.; Soudackov, A. V.; Zhang, H.; Krumov, M.; Murray, E.; Xu, P.; Hitt, J.; Xu, L.; Ko, H. Y.; Ernst, B. G.; Bundschu, C.; Luo, A.; Markovich, D.; Hu, M.; He, C.; Wang, H.; Fang, J.; DiStasio, R. A.; Kourkoutis, L. F.; Singer, A.; Noonan, K. J. T.; Xiao, L.; Zhuang, L.; Pivovar, B. S.; Zelenay, P.; Herrero, E.; Feliu, J. M.; Suntivich, J.; Giannelis, E. P.; Hammes-Schiffer, S.; Arias, T.; Mavrikakis, M.; Mallouk, T. E.; Brock, J. D.; Muller, D. A.; DiSalvo, F. J.; Coates, G. W.; Abruna, H. D. Electrocatalysis in Alkaline Media and Alkaline Membrane-Based Energy Technologies. *Chem. Rev.* **2022**, *122*, 6117−6321.
(33) Yang, X.; Wang, Y.; Tong, X.; Yang, N. Strain Engineering in Electrocatalysts: Fundamentals, Progress, and Perspectives. *Adv. Energy Mater.* **2022**, *12*, No. 2102261.
(34) Wu, G.; Han, X.; Cai, J.; Yin, P.; Cui, P.; Zheng, X.; Li, H.; Chen, C.; Wang, G.; Hong, X. In-plane Strain Engineering in Ultrathin Noble Metal Nanosheets Boosts the Intrinsic Electrocatalytic ydrogen Evolution Activity. *Nat. Commun.* **2022**, *13*, 4200.
(35) Mukherjee, D.; Gamler, J. T. L.; Skrabalak, S. E.; Unocic, R. R. Lattice Strain Measurement of Core@Shell Electrocatalysts with 4D Scanning Transmission Electron Microscopy Nanobeam Electron Diffraction. *ACS Catal.* **2020**, *10*, 5529−5541.
(36) Sarkar, S.; Ramarao, S. D.; Das, T.; Das, R.; Vinod, C. P.; Chakraborty, S.; Peter, S. C. Unveiling the Roles of Lattice Strain and Descriptor Species on Pt-Like Oxygen Reduction Activity in Pd−Bi Catalysts. *ACS Catal.* **2021**, *11*, 800−808.
(37) Topalian, P. J.; Liyanage, D. R.; Danforth, S. J.; d'Aquino, A. I.; Brock, S. L.; Bussell, M. E. Effect of Particle Size on the Deep HDS Properties of Ni_2P Catalysts. *J. Phys. Chem. C* **2019**, *123*, 25701−25711.
(38) Lin, C.-C.; Guo, Y.; Vela, J. Microstructure Effects on the Water Oxidation Activity of Co_3O_4/Porous Silica Nanocomposites. *ACS Catal.* **2015**, *5*, 1037−1044.
(39) Huang, R.; Luo, L.; Hu, W.; Tang, Z.; Ji, X.; Chen, L.; Yu, Z.; Zhang, Y.; Zhang, D.; Xiao, P. Insight into the pH Effect on the Oxygen Species and Mn Chemical Valence of Co−Mn Catalysts for Total Toluene Oxidation. *Catal. Sci. Technol.* **2022**, *12*, 4157−4168.
(40) van Embden, J.; Chesman, A. S. R.; Jasieniak, J. J. The Heat-Up Synthesis of Colloidal Nanocrystals. *Chem. Mater.* **2015**, *27*, 2246−2285.
(41) Kwon, S. G.; Hyeon, T. Formation Mechanisms of Uniform Nanocrystals via Hot-injection and eat-up Methods. *Small* **2011**, *7*, 2685−2702.
(42) Sun, S.; Zeng, H.; Robinson, D. B.; Raoux, S.; Rice, P. M.; Wang, S. X.; Li, G. Monodisperse MFe_2O_4 (M = Fe, Co, Mn) Nanoparticles. *J. Am. Chem. Soc.* **2004**, *126*, 273−279.
(43) Plummer, L. K.; Hutchison, J. E. Understanding the Effects of Iron Precursor Ligation and Oxidation State Leads to Improved Synthetic Control for Spinel Iron Oxide Nanocrystals. *Inorg. Chem.* **2020**, *59*, 15074−15087.
(44) Pinna, N.; Garnweitner, G.; Antonietti, M.; Niederberger, M. A General Nonaqueous Route to Binary Metal Oxide Nanocrystals Involving a C-C Bond Cleavage. *J. Am. Chem. Soc.* **2005**, *127*, 5608−5612.
(45) Chang, H.; Kim, B. H.; Lim, S. G.; Baek, H.; Park, J.; Hyeon, T. Role of the Precursor Composition in the Synthesis of Metal Ferrite Nanoparticles. *Inorg. Chem.* **2021**, *60*, 4261−4268.
(46) Cabot, A.; Puntes, V. F.; Shevchenko, E.; Yin, Y.; Balcells, L.; Marcus, M. A.; Hughes, S. M.; Alivisatos, A. P. Vacancy Coalescence During Oxidation of Iron Nanoparticles. *J. Am. Chem. Soc.* **2007**, *129*, 10358−10360.
(47) Sanchez-Lievanos, K. R.; Knowles, K. E. Controlling Cation Distribution and Morphology in Colloidal Zinc Ferrite Nanocrystals. *Chem. Mater.* **2022**, *34*, 7446−7459.
(48) Sanchez-Lievanos, K. R.; Tariq, M.; Brennessel, W. W.; Knowles, K. E. Heterometallic Trinuclear Oxo-centered Clusters as Single-source Precursors for Synthesis of Stoichiometric Monodisperse Transition Metal Ferrite Nanocrystals. *Dalton Trans.* **2020**, *49*, 16348−16358.
(49) Bard, A. J.; Faulkner, L. R.; White, H. S. *Electrochemical Methods: Fundamentals and Applications*; John Wiley & Sons, 2022.
(50) Ito, D.; Yokoyama, S.; Zaikova, T.; Masuko, K.; Hutchison, J. E. Synthesis of Ligand-stabilized Metal Oxide Nanocrystals and Epitaxial Core/shell Nanocrystals via a Lower-temperature Esterification Process. *ACS Nano* **2014**, *8*, 64−75.
(51) Niederberger, M.; Bartl, M. H.; Stucky, G. D. Benzyl Alcohol and Titanium TetrachlorideA Versatile Reaction System for the Nonaqueous and Low-Temperature Preparation of Crystalline and Luminescent Titania Nanoparticles. *Chem. Mater.* **2002**, *14*, 4364−4370.
(52) Zhang, H. T.; Chen, X. H. Size-dependent X-ray Photoelectron Spectroscopy and Complex Magnetic Properties of $CoMn_2O_4$ Spinel Nanocrystals. *Nanotechnology* **2006**, *17*, 1384−1390.
(53) Parvizian, M.; Duran Balsa, A.; Pokratath, R.; Kalha, C.; Lee, S.; Van den Eynden, D.; Ibanez, M.; Regoutz, A.; De Roo, J. The Chemistry of Cu_3N and Cu_3PdN Nanocrystals. *Angew. Chem., Int. Ed.* **2022**, *61*, No. e202207013.
(54) Calcabrini, M.; Van den Eynden, D.; Ribot, S. S.; Pokratath, R.; Llorca, J.; De Roo, J.; Ibáñez, M. Ligand Conversion in Nanocrystal Synthesis: The Oxidation of Alkylamines to Fatty Acids by Nitrate. *JACS Au* **2021**, *1*, 1898−1903.
(55) Moulder, J. F.; Stickle, W. F.; Sobol, P. E.; Bomben, K. D. *Handbook of X-ray Photoelectron Spectroscopy*; Perkin-Elmer Corporation, 1992.
(56) Biesinger, M. C.; Payne, B. P.; Grosvenor, A. P.; Lau, L. W. M.; Gerson, A. R.; Smart, R. S. C. Resolving Surface Chemical States in XPS Analysis of First Row Transition Metals, Oxides and Hydroxides: Cr, Mn, Fe Co and Ni. *Appl. Surf. Sci.* **2011**, *257*, 2717−2730.
(57) Huang, H.; Shen, B.; Yan, M.; He, H.; Yang, L.; Jiang, Q.; Ying, G. Coupled Spinel Manganese−cobalt Oxide and MXene Electrocatalysts Towards Efficient Hydrogen Evolution Reaction. *Fuel* **2022**, *328*, No. 125234.
(58) Ramírez, A.; Hillebrand, P.; Stellmach, D.; May, M. M.; Bogdanoff, P.; Fiechter, S. Evaluation of MnO_x, Mn_2O_3, and Mn_3O_4 Electrodeposited Films for the Oxygen Evolution Reaction of Water. *J. Phys. Chem. C* **2014**, *118*, 14073−14081.
(59) Kong, X.; Zhu, T.; Cheng, F.; Zhu, M.; Cao, X.; Liang, S.; Cao, G.; Pan, A. Uniform $MnCo_2O_4$ Porous Dumbbells for Lithium-Ion Batteries and Oxygen Evolution Reactions. *ACS Appl. Mater. Interfaces* **2018**, *10*, 8730−8738.
(60) Peng, Y.; Si, W.; Luo, J.; Su, W.; Chang, H.; Li, J.; Hao, J.; Crittenden, J. Surface Tuning of $La_{0.5}Sr_{0.5}CoO_3$ Perovskite Catalysts by Acetic Acid for NO_x Storage and Reduction. *Environ. Sci. Technol.* **2016**, *50*, 6442−6448.
(61) Xie, W.; Xu, G.; Zhang, Y.; Yu, Y.; He, H. Mesoporous $LaCoO_3$ Perovskite Oxide with High Catalytic Performance for NO_x Storage and Reduction. *J. Hazard. Mater.* **2022**, *431*, No. 128528.
(62) Anderson, N. C.; Hendricks, M. P.; Choi, J. J.; Owen, J. S. Ligand Exchange and the Stoichiometry of Metal Chalcogenide Nanocrystals: Spectroscopic Observation of Facile Metal-carboxylate Displacement and Binding. *J. Am. Chem. Soc.* **2013**, *135*, 18536−18548.

(63) Drijvers, E.; De Roo, J.; Martins, J. C.; Infante, I.; Hens, Z. Ligand Displacement Exposes Binding Site Heterogeneity on CdSe Nanocrystal Surfaces. *Chem. Mater.* **2018**, *30*, 1178−1186.
(64) Kessler, M. L.; Kelm, J. E.; Starr, H. E.; Cook, E. N.; Miller, J. D.; Rivera, N. A.; Hsu-Kim, H.; Dempsey, J. L. Unraveling Changes to PbS Nanocrystal Surfaces Induced by Thiols. *Chem. Mater.* **2022**, *34*, 1710−1721.
(65) Morris-Cohen, A. J.; Frederick, M. T.; Lilly, G. D.; McArthur, E. A.; Weiss, E. A. Organic Surfactant-Controlled Composition of the Surfaces of CdSe Quantum Dots. *J. Phys. Chem. Lett.* **2010**, *1*, 1078−1081.
(66) Hughes, B. K.; Ruddy, D. A.; Blackburn, J. L.; Smith, D. K.; Bergren, M. R.; Nozik, A. J.; Johnson, J. C.; Beard, M. C. Control of PbSe Quantum Dot Surface Chemistry and Photophysics using an Alkylselenide Ligand. *ACS Nano* **2012**, *6*, 5498−5506.
(67) Akkerman, Q. A.; Nguyen, T. P. T.; Boehme, S. C.; Montanarella, F.; Dirin, D. N.; Wechsler, P.; Beiglböck, F.; Rainò, G.; Erni, R.; Katan, C.; Even, J.; Kovalenko, M. V. Controlling the Nucleation and Growth Kinetics of Lead Halide Perovskite Quantum Dots. *Science* **2022**, *377*, 1406−1412.
(68) Tappan, B. A.; Horton, M. K.; Brutchey, R. L. Ligand-Mediated Phase Control in Colloidal $AgInSe_2$ Nanocrystals. *Chem. Mater.* **2020**, *32*, 2935−2945.
(69) Wang, F.; Tang, R.; Buhro, W. E. The Trouble with TOPO; Identification of Adventitious Impurities Beneficial to the growth of cadmium selenide quantum dots, rods, and wires. *Nano Lett.* **2008**, *8*, 3521−3524.
(70) Peng, J.; Giordano, L.; Davenport, T. C.; Shao-Horn, Y. Stability Design Principles of Manganese-Based Oxides in Acid. *Chem. Mater.* **2022**, *34*, 7774−7787.
(71) Braddock, D. C.; Davies, J. J.; Lickiss, P. D. Methyltrimethoxysilane (MTM) as a Reagent for Direct Amidation of Carboxylic Acids. *Org. Lett.* **2022**, *24*, 1175−1179.
(72) Nishinaga, A.; Yamazaki, S.; Matsuura, T. Catalytic Dehydrogenation of Secondary Amines with Cobalt Schiff Base Complex-oxygen System. *Tetrahedron Lett.* **1988**, *29*, 4115−4118.
(73) Khanna, H. S.; Eddy, N. A.; Dang, Y.; Bhosale, T. S.; Shubhashish, S.; Suib, S. L.; Nandi, P. Nanoporous Co/Mn-Mixed Metal Oxides Templated via Polysulfones for Amine Oxidation. *ACS Appl. Nano Mater.* **2020**, *3*, 11923−11932.
(74) Hazra, S.; Pilania, P.; Deb, M.; Kushawaha, A. K.; Elias, A. J. Aerobic Oxidation of Primary Amines to Imines in Water using a Cobalt Complex as Recyclable Catalyst under Mild Conditions. *Chemistry* **2018**, *24*, 15766−15771.
(75) Biswas, S.; Dutta, B.; Mullick, K.; Kuo, C.-H.; Poyraz, A. S.; Suib, S. L. Aerobic Oxidation of Amines to Imines by Cesium-Promoted Mesoporous Manganese Oxide. *ACS Catal.* **2015**, *5*, 4394−4403.
(76) Cui, X.; Li, W.; Junge, K.; Fei, Z.; Beller, M.; Dyson, P. J. Selective Acceptorless Dehydrogenation of Primary Amines to Imines by Core−Shell Cobalt Nanoparticles. *Angew. Chem., Int. Ed.* **2020**, *59*, 7501−7507.
(77) Brown, J. F., Jr. The Infrared Spectra of Nitro and Other Oxidized Nitrogen Compounds. *J. Am. Chem. Soc.* **1955**, *77*, 6341−6351.
(78) Pesesse, A.; Carenco, S. Influence of the Copper Precursor on the Catalytic Transformation of Oleylamine During Cu Nanoparticle Synthesis. *Catal. Sci. Technol.* **2021**, *11*, 5310−5320.
(79) Wheeler, O. H.; Gonzalez, D. Oxidation of Primary Aromatic Amines with Manganese Dioxide. *Tetrahedron* **1964**, *20*, 189−193.
(80) Chang, C.-F.; Liu, S.-T. Catalytic Oxidation of Anilines into Azoxybenzenes on Mesoporous Silicas Containing Cobalt Oxide. *J. Mol. Catal. A: Chem.* **2009**, *299*, 121−126.
(81) Morris-Cohen, A. J.; Donakowski, M. D.; Knowles, K. E.; Weiss, E. A. The Effect of a Common Purification Procedure on the Chemical Composition of the Surfaces of CdSe Quantum Dots Synthesized with Trioctylphosphine Oxide. *J. Phys. Chem. C* **2010**, *114*, 897−906.
(82) Owen, J. S.; Park, J.; Trudeau, P. E.; Alivisatos, A. P. Reaction Chemistry and Ligand Exchange at Cadmium-selenide Nanocrystal Surfaces. *J. Am. Chem. Soc.* **2008**, *130*, 12279−12281.
(83) Moreels, I.; Lambert, K.; De Muynck, D.; Vanhaecke, F.; Poelman, D.; Martins, J. C.; Allan, G.; Hens, Z. Composition and Size-Dependent Extinction Coefficient of Colloidal PbSe Quantum Dots. *Chem. Mater.* **2007**, *19*, 6101−6106.
(84) Baymou, Y.; Bidi, H.; Ebn Touhami, M.; Allam, M.; Rkayae, M.; Belakhmima, R. A. Corrosion Protection for Cast Iron in Sulfamic Acid Solutions and Studies of the Cooperative Effect Between Cationic Surfactant and Acid Counterions. *J. Bio- Tribo-Corros.* **2018**, *4*, 11.
(85) Iannuzzi, M.; Young, T.; Frankel, G. S. Aluminum Alloy Corrosion Inhibition by Vanadates. *J. Electrochem. Soc.* **2006**, *153*, B533.

https://doi.org/10.1021/jacs.3c05706
J. Am. Chem. Soc. 2023, 145, 17406−17419